Earth Planet. Sci. Lett. 637 (2024) 118699

Contents lists available at ScienceDirect

Earth and Planetary Science Letters

journal homepage: www.elsevier.com/locate/epsl

The combined effect of heterogeneous thermal conductivity, chemical density contrast, and heat-producing element enrichment on the stability of primordial reservoirs above the core-mantle boundary

J.M. Guerrero [a,*], F. Deschamps [a,*], Wen-Pin Hsieh [a], P.J. Tackley [b]

[a] Institute of Earth Sciences, Academia Sinica, 128, Sec. 2, Academia Road, Nangang, Taipei 11529, Taiwan
[b] Department of Earth Sciences, ETH Zürich, Sonneggstrasse 5, 8092 Zürich, Switzerland

ARTICLE INFO

Editor: J. Badro

Keywords:
mantle convection
thermal conductivity
primordial reservoir
heat-producing element
buoyancy ratio

ABSTRACT

Earth's deep mantle hosts continental-scale enigmatic structures whose origin, characteristics, and fate are uncovered by advances in tomographic modeling, geochemical analysis, measurements of mantle mineral properties under extreme conditions, and novel methods in mantle convection modeling. Probabilistic tomography revealed that these deep mantle structures, dubbed large low shear velocity provinces (LLSVPs), are likely enriched in iron-bearing bridgmanite, making them denser than the surrounding ambient mantle (establishing a stabilizing negative buoyancy). A distinct geochemical signature observed in ocean-island basalts is thought to be sourced from the deep mantle, which indicates that LLSVPs may be candidates for a primordial reservoir enriched in heat-producing elements (promoting a destabilizing positive buoyancy). Using conductivity measurements from upper and lower mantle minerals, we derived a novel parametrized depth-, temperature-, and composition-dependent thermal conductivity model. With thermochemical mantle convection models, we demonstrated how the thermal state and total buoyancy of primordial reservoirs (as an analogue for LLSVPs) are influenced by a dynamically responsive and (spatially, thermally, and compositionally) heterogeneous thermal conductivity field. We examined the influence of moderate to high temperature-dependent conductivity models on the evolution of primordial reservoirs characterized by intrinsic chemical density contrast between 1.5 and 5% and heat-producing element (HPE) enrichment factors between 1 and 20. The lowermost mantle attains mean conductivities of ~ 6 W/m/K within reservoirs and ~ 9 W/m/K outside for moderate temperature dependence. For a high temperature dependence, mean conductivities are reduced to ~ 2 W/m/K and ~ 5 W/m/K, respectively. We found that heterogeneous thermal conductivity exacerbates the thermally driven effect of HPE enrichment, and the strength of the thermal contribution to the total conductivity is decisive in determining the long-term stability (> 10 Gyr of simulation time) of primordial reservoirs. For the parameter space we consider, the stability of primordial reservoirs with a particular HPE factor improves with greater density contrast. However, with a particular density contrast, stability decreases with a greater HPE factor. Thus, pile instability occurs for a combination of parameters that promote the domination of thermal buoyancy over chemical buoyancy. For a moderate HPE enrichment (factor of 10) and a highly temperature-dependent conductivity, reservoirs characterized by a density contrast ~ 4% attain a mean density ~ 1.4% and achieve long-term stability. For a moderately temperature-dependent conductivity, reservoirs characterized by a density contrast ~ 3% attain a mean density ~ 1.0%, consistent with tomographic estimates of LLSVP density and achieving long-term stability. When HPE enrichment is present, we found that a greater thermal buoyancy is more likely when temperature dependence is stronger due to the piles' larger temperature. Thus, a greater intrinsic chemical density contrast is required to maintain stable and long-lived primordial reservoirs.

* Corresponding authors.
E-mail addresses: joshua@earth.sinica.edu.tw (J.M. Guerrero), frederic@earth.sinica.edu.tw (F. Deschamps).

https://doi.org/10.1016/j.epsl.2024.118699
Received 5 October 2023; Received in revised form 26 February 2024; Accepted 4 April 2024

1. Introduction

The large low shear velocity provinces (LLSVPs) mapped by seismic tomography at the base of the Earth's mantle are likely hotter than and chemically differentiated from the regular mantle (see Garnero et al. (2016) for a review). The fate of these regions depends on the competition between their intrinsic chemical density anomaly (negative buoyancy) and thermal density anomaly (positive buoyancy). When the dynamics of these regions are negative-buoyancy dominated, the hot but chemically dense material forms relatively flat structures on the core-mantle boundary (CMB), and the pattern of downwelling currents originating at the Earth's surface influences lateral motion and organizes dense material into piles. When the dynamics are positive-buoyancy dominated, the hot and less dense thermal anomalies can generate thermochemical plumes within piles, and downwelling flow generates thermochemical plumes at the top and edges of chemically dense piles. Specifically, from finer resolution tomographic modeling, our interpretation of pile-like structures could be interpreted as poorly resolved plume-bundles (e.g., Davaille and Romanowicz, 2020) and from mantle flow reconstruction, the lateral evolution of basal mantle structures is similar to continents on the Earth's surface (e.g., Flament et al., 2022). The buoyancy of LLSVPs depends on their exact chemical compositions and heat-producing element (HPE) enrichment, both of which are not well known. While many combinations of composition and enrichment are plausible, the mechanisms defining positive and negative buoyancy sources differ; thus, even for differing combinations of physical parameters for which the total buoyancy is identical, the resulting evolution and overall distribution of thermochemical material determined by their competing dynamics will be unique.

The physical properties of LLSVPs depend on their composition and, hence, their origin and formation. The two end-member hypotheses include recycled crustal material (MORB) and remnant primordial material from the crystallization of a basal magma ocean (Tackley, 2012). In numerical modeling, while both origin treatments are geodynamically able to produce long-lived piles, a primordial composition fits the seismic signature of Earth's large low-shear wave velocity provinces (Deschamps et al., 2012). However, we do not rule out the possibility of MORB in LLSVPs (e.g., Li and McNamara, 2013, 2022). Enrichment in iron and bridgmanite contributes to piles' higher density and lower conductivity relative to the ambient mantle (Deschamps and Hsieh, 2019). A buoyancy ratio, B, which is the ratio of the chemical density difference between primordial and ambient mantle minerals versus the thermal density difference (defined in Equation (5)), is often used to characterize compositional density contrasts in numerical or experimental models. For Earth's lower mantle, a 3% iron and 18% (Mg,Fe)-perovskite composition results in an approximate chemical density contrast of 152 kg/m^3 (corresponding to $B = 0.23$). This chemical density contrast directly controls the basal mantle structure, and values smaller or larger than this reference value can result in entrainment or stable layering of primordial material, respectively.

The net (i.e., thermal and chemical) density estimates of LLSVPs (combining both compositional and thermal contributions) depend on the method of estimation or observation. From probabilistic tomography and normal-mode studies, first-order estimates place the chemical density contrast between 0.5 and 1% (e.g., Resovsky and Trampert, 2003; Trampert et al., 2004; Mosca et al., 2012). From the analysis of high-resolution tomographic images, Davaille and Romanowicz (2020) propose that bundles of low shear-wave velocity plumes are consistent with the dome-like structure of LLSVPs inferred from low-resolution tomographic images. Across the bottom two-thirds of LLSVPs, tidal tomography places the mean density 0.5% higher than the average mantle density at the same depth range (Lau et al., 2017). In contrast, based on Stoneley mode splitting measurements, Koelemeijer et al. (2017) report an overall density reduction of 0.88% but do not rule out the possibility of a denser basal mantle structure in the lowermost 100 km. Despite the disagreement between Stoneley mode studies and other methods for estimating the LLSVPs' density, the consensus is that density variations relative to the ambient mantle are about 2% or less.

Experimental or numerical models help constrain the density of LLSVPs by trying to reproduce their observed characteristics. Early geodynamics studies show that a stable deep thermochemical layer (with significant topography) is long-lived over the age of the Earth when the density contrast is 4% or more (van der Hilst and Kárason, 1999; Kellogg et al., 1999). Later studies showed that a chemical density contrast of 2.4% is sufficient to produce a deep stable layer (Samuel and Farnetani, 2003). In addition to maintaining a deep stable layer, the morphology of this dense material depends on the density contrast. For low density contrasts (< 1%), the thermochemical structure takes on a dome or superplume morphology (Davaille, 1999) and for greater density contrasts (1 - 2%), a pile-like morphology is observed (Tackley, 1998).

Furthermore, the long-term stability of piles has routinely been examined for thermochemical piles as a function of their composition, viscosity, internal heating, and other physical parameters in combination with chemical density contrast (e.g., Li et al., 2014; Limare et al., 2019; Citron et al., 2020; Huang et al., 2022). In general, the chemical density contrast is the primary parameter governing the stability of thermochemical piles. For a wide range of additional physical parameters, density contrasts between 1 and 3% result in long-lived thermochemical piles. Below this range of densities, thermochemical piles become entrained. Greater than this range, thermochemical piles can maintain a wide and flat topography, and thermochemical convection can be considered layered.

Similar to the density distribution in the mantle, the amount and distribution of HPEs are uncertain and depend on the composition of the mantle. A deep mantle reservoir is supported by geochemical observations of ocean island basalts (OIBs), which exhibit high He^3/He^4 ratio signatures suggesting that this source has not mixed with regular mantle-sourced material. Arevalo et al. (2013) estimate that the OIB source is 19% of the mantle by mass. Based on the approach of Šrámek et al. (2013) and assuming that LLSVPs occupy 9% of the mantle by mass (Cottaar and Lekic, 2016), Citron et al. (2020) estimate that the present-day heat production within the reservoir could be approximately 10 to 100 times higher than the ambient mantle. Heat-producing element enrichment directly controls the basal mantle structures' temperature (and hence, thermal buoyancy) and, thus, their long-term stability. Citron et al. (2020) found that a stable pile-like morphology is possible for a dense layer with HPE enrichment. In addition, for given B and dH_{prim}, accounting for decaying internal heat sources slightly modifies the pile morphology regimes compared to constant heating cases. Huang et al. (2022) recently found that differences in pile stability regimes are marginally affected by considering time-dependent decaying heat sources. Depending on the decay rate or the aggregate composition of HPEs in mantle material, models considering decaying heat sources imply an initial internal heating rate of approximately 3 to 5 times the present-day value. Naturally, a greater radiogenic heat production at the start of a mantle convection simulation, in combination with heat-producing element enrichment, will make piles more thermally buoyant and further expose the CMB surface area. However, these studies had not considered variable thermal conductivity that may act to exacerbate the destabilizing thermal effect brought on by HPE enrichment. Here, we reevaluate these findings in a new context of heterogeneous thermal conductivity.

Experimental studies on mantle minerals show that their thermal conductivities are sensitive to variations in pressure (depth), temperature, and composition. At a fixed temperature, thermal conductivities increase with increasing pressure, with typical lowermost mantle conductivities exceeding five times the surface conductivity value (e.g., Dalton et al., 2013; Hsieh et al., 2017, 2018). At a fixed pressure, thermal conductivities decrease with increasing temperature (e.g., Hofmeister, 1999; Manthilake et al., 2011; Zhang et al., 2019). For example, assuming a moderate temperature dependence, a temperature

of 3000 K, typical of the lowermost mantle, results in a ~70% reduction in conductivity relative to material with a temperature of 300 K at lowermost mantle pressure. Including iron or aluminum in mantle minerals substantially reduces thermal conductivity relative to their purely magnesium compositions (e.g., Ohta et al., 2012; Hsieh et al., 2017, 2018). Not only does this curb the thermal conductivity of the mantle at higher pressures, but the thermal conductivity of lowermost mantle structures enriched in iron or aluminum-bearing bridgmanite (i.e., LLSVPs) may be significantly reduced relative to the ambient mantle at the same pressure. Measurements of thermal conductivities at lower mantle conditions are few, and the conductivity of piles is even less well-constrained. Because thermal conductivity regulates heat flow, it partially controls the temperature and, hence, thermal buoyancy and stability of the anomalously dense regions at the base of the mantle. Although thermal conductivity's precise temperature dependence in the lower mantle remains uncertain, for piles with an intrinsic chemical density contrast characteristic of LLSVPs, even a weak temperature dependence combined with heat-producing element enrichment can promote entrainment.

Recently, Guerrero et al. (2023) showed that the ratio between the bottom and top conductivities implied by the system's combined conductivity dependencies controls the growth of temperature anomalies within thermochemical piles and determines the onset of thermal instability. If the system can establish a higher conductivity in the lowermost mantle (e.g., if the depth-dependent increase exceeds the temperature-dependent decrease in conductivity), a moderately conductive thermochemical pile can rid itself of excess heat, be cooled by the ambient mantle surrounding it and remain stable. If not, a poorly conducting thermochemical pile cannot easily rid itself of its excess heat, become even more poorly conducting (establishing a positive feedback loop), and hence thermally unstable. The depth-dependent conductivity deduced from upper and lower mantle conductivity measurements (Deschamps and Hsieh, 2019), in conjunction with moderate temperature and compositional dependences, produces an antipodal two-pile configuration consistent with observations. Simulations showed that a sub-unity bottom-to-top conductivity ratio results in the growth of instability within piles. However, our examination of the stability of lower mantle thermochemical structure was limited to a single buoyancy ratio and HPE enrichment factor. This study investigates the combined effects of heterogeneous thermal conductivity, buoyancy ratio, and HPE enrichment on the dynamics and evolution of dense thermochemical anomalies of primordial origin.

2. Method

2.1. Numerical approach

We solve the non-dimensional forms of the conservation equations of momentum, mass, energy and composition for a compressible, infinite Prandtl number fluid using the finite volume code StagYY (Tackley, 2008). The numerical setup is similar to that in Guerrero et al. (2023) and is summarized in the appendix and supplemental material, including details regarding the governing equations, governing parameters, system variables, and material properties. Given that the evolution of primordial reservoirs is the focus of our study, the governing parameters examined include the buoyancy ratio B and the internal heating rate enrichment factor dH_{prim} (emulating HPE enrichment within piles). Variations in the mantle's thermal conductivity, k, are examined to systematically investigate the evolution of thermochemical primordial reservoirs in combination with B and dH_{prim}. Fig. 1 shows radial profiles for the temperature field and primordial field initial conditions and for the thermal conductivity model employed in this study. Again, we model heterogeneous conductivity following the approach of Guerrero et al. (2023), which we summarize in the next paragraph.

2.2. Thermal conductivity

We use a non-dimensional parametrized model that characterizes variations resulting from non-dimensional depth, $\tilde{d} = d/D$, where the depth, d, has a length scale defined by the mantle thickness, D; non-dimensional temperature, $\tilde{T} = T/\Delta T_S$, where the temperature, T, is scaled by the super-adiabatic temperature difference, ΔT_S; and composition, C; as separate functions. Thermal conductivity is non-dimensionalized with its surface value k_{Surf}, which is here fixed to 3 W/m/K. The total conductivity is a product of each functional dependence.

First we consider a conductivity parametrization purely based on a linear depth-dependent profile. The conductivity profile is defined by a linear function, $\tilde{k}_D(\tilde{d}) = 1 + (K_D - 1)\tilde{d}$, where K_D controls the conductivity value at the core-mantle boundary. Because this function is defined non-dimensionally, the ratio of the bottom and top conductivity is simply determined by K_D value. Fig. 1(b) shows radial profiles for cases featuring $K_D = 2.5$, 5.0, and 10.0. By considering this simple conductivity model, we can isolate the combined effect of buoyancy ratio and bottom-to-top conductivity ratio, on the evolution of primordial reservoirs.

Next, we consider a heterogeneous thermal conductivity parametrization where the depth-dependence is based on conductivity measurements of upper and lower mantle minerals (Chang et al., 2017; Hsieh et al., 2017, 2018; Deschamps and Hsieh, 2019). The conductivity profile in the upper mantle is defined by a quadratic curve that smoothly connects the surface conductivity to the conductivity profile of Bm-Fp at the 660-km transition. The total conductivity profile, denoted by the symbol K_{DH} (Fig. 1(b), blue curve), is defined piecewise and continuous at the 660-km transition ($\tilde{d}_{ULM} = 0.22837$) and is given by

$$\tilde{k}_D(\tilde{d}) = \begin{cases} \frac{3.0}{k_{Surf}}\left(1 + 15.66\tilde{d} - 16.38\tilde{d}^2\right); & \tilde{d} < \tilde{d}_{ULM} \quad \text{(Upper mantle)} \\ \frac{5.33}{k_{Surf}}\left(1 + 4.98\tilde{d} - 0.81\tilde{d}^2\right); & \tilde{d} \geq \tilde{d}_{ULM} \quad \text{(Lower mantle).} \end{cases} \tag{1}$$

Temperature-dependence is given by

$$\tilde{k}_T(\tilde{T}) = \left(\frac{(T_{Surf}/\Delta T_S)}{\tilde{T}}\right)^n, \tag{2}$$

where the surface temperature, T_{Surf}, is set to 300 K, and the super-adiabatic temperature difference, ΔT_S, is set to 2500 K. Temperature-dependence always results in lower conductivity. Higher values of n indicate higher sensitivity to (and thus more significant reduction with) increasing temperature. In this study, we consider n values of 0.5 and 0.8. The theoretical lower limit for n is 0.5 for materials enriched in iron, and 0.8 is representative of oxide-bearing minerals (e.g., Klemens, 1960; Xu et al., 2004). When $n = 0.0$, temperature-dependence is switched off, and only the remaining dependencies are considered.

Composition-dependence is given by

$$\tilde{k}_C(C) = 1 + (K_C - 1)C \tag{3}$$

where K_C is the reduction factor for composition-dependence. In this study, we consider $K_C = 0.8$ (corresponding to a 20% conductivity reduction), which is consistent with the inferred conductivity of LLSVP regions modeled by Deschamps and Hsieh (2019). Finally, the total conductivity is given by

$$k(d, T, C) = k_{Surf} \times \tilde{k}_D(d) \times \tilde{k}_T(T) \times \tilde{k}_C(C). \tag{4}$$

Fig. 1(c) demonstrates the effect of temperature- and composition-dependence for simulations featuring a depth-dependence defined by Equation (1). According to our temperature field, a temperature dependence featuring $n = 0.5$ results in a 70% reduction and $n = 0.8$ results in a 86% reduction at the core-mantle boundary. The absolute value

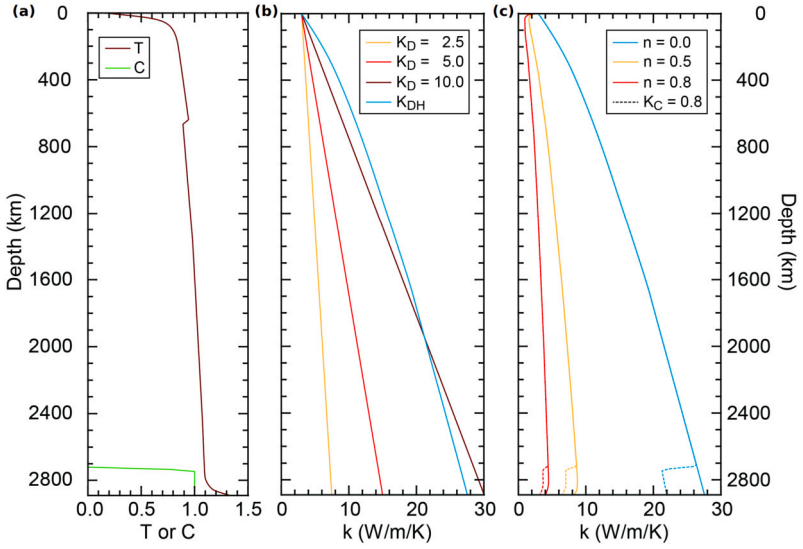

Fig. 1. (a) Non-dimensional radial profiles for the initial temperature field (brown) and primordial material field (green). Temperature is dimensionalized by multiplying with the super-adiabatic temperature difference, ΔT_S. (b) Radial profiles for depth-dependent conductivity functions defined linearly with slope characterized by K_D and by a parameterization derived from conductivity measurements in the upper and lower mantle by Deschamps and Hsieh (2019) (denoted by K_{DH}). (c) Initial radial profiles for conductivity models featuring different temperature- and composition-dependencies.

of conductivity reduction due to the composition dependence decreases when the slope of the total conductivity profile is smaller.

2.3. Buoyancy ratio

Because primordial material is enriched in heavier minerals, it is assumed to be denser than regular (pyrolytic) mantle material. In our model, the chemical density contrast between both materials is defined with respect to the reference density profile, $\rho(z)$, and is given by $B\alpha_{Surf}\Delta T_S\rho(z)$ (e.g., Deschamps et al., 2018). Thus, the buoyancy ratio defined by

$$B = \frac{\Delta\rho_C(z)}{\alpha_{Surf}\rho_{\text{ref}}(z)\Delta T_S}, \tag{5}$$

is fixed at a constant value. Compared with models with B defined with respect to the surface density, the buoyancy ratios required for stable chemical stratification will be smaller. More generally, whatever the definition of the buoyancy ratio, thermo-chemical structures obtained with equivalent chemical density contrast at the bottom of the system are very similar. Nevertheless, our buoyancy ratio definition produces density differences that are consistent with estimates of the intrinsic density of contrast between primordial and ambient mantle material (e.g., 2 - 2.8%). Here, we prescribed values of B between 0.15 and 0.40, which encompass the range of density contrasts that are characteristic of LLSVPs and correspond to values in the range 90-250 kg/m^3.

2.4. Model setup

We perform each simulation in a 2D spherical annulus domain, which emulates convection in a variable-thickness slice of a spherical shell centered at the equator (Hernlund and Tackley, 2008). All parameters and dimensional scales for our thermochemical mantle convection model are listed in Table 1. A curvature factor $f = 0.55$ (calculated from the ratio of CMB radius to surface radius) characterizes an Earth-like mantle geometry, and we subdivide the domain into 128-node radial and 2048-node lateral resolution. We specify additional grid refinement at the surface and core-mantle boundaries and the 660-km transition to ensure the flow is resolved well in those regions. The annulus domain features free-slip surface and core-mantle boundaries. Relative to a surface temperature of 300 K, the reference state (see Figure S1) determines a CMB temperature of 3440 K. The initial condition for the temperature field is radially symmetric and based on an adiabatic temperature of 2000 K with surface and core-mantle boundary layer thicknesses of approximately 30 km. Random temperature perturbations with an amplitude of 125 K are uniformly distributed throughout the domain. The initial condition for the primordial field is also radially symmetric and defined by a uniform dense layer on top of the core-mantle boundary with a thickness of 160 km. Under this setup, an initial transient phase lasting approximately 1.0 to 2.0 Gyr (depending on the conductivity model employed) is observed during which the bottom of the mantle heats up and the first downwellings impinge on the initial dense layer.

We run simulations over a non-dimensional diffusion time of 0.0318, corresponding to 11.2 Gyr in dimensional units. Note that because they do not include Earth's mantle initial conditions, which are anyway not well constrained, and time-decreasing radioactive heating, our simulations are not designed to model the Earth's evolution. Therefore, durations should not be used to interpret specific sequences of events. The longer simulation time is necessary to allow the simulations to achieve a quasi-steady state, during which the surface and CMB heat flow oscillate around nearly constant values. The appendix and supplemental material contain the complete details of the methods.

3. Results

Using the setup defined in the methods section, we run 52 cases sampling B and dH_{prim} in the range of 0.15-0.40 and 1-20, respectively and for temperature-dependent conductivity with $n = 0.5$ and 0.8 (Table 2). Output observable and derived properties are averaged over a 1 Gyr window about $t = 4.5$ Gyr. These simulations highlight tradeoffs between conductivity changes and physical parameters, leading to constructive or complementary effects on pile properties.

3.1. Buoyancy ratio versus depth-dependence of conductivity

We first examine the effect of the bottom-to-top conductivity ratio (K_D) and buoyancy ratio (B). Conductivity values at the CMB correspond to 7.5, 15, and 30 W/m/K for $K_D = 2.5, 5$, and 10, respectively. By comparison, the predicted pyrolite conductivities near the CMB (including thermal effects) are around 8-10 W/m/K. Considering an adiabatic and super-adiabatic temperature increase leads to a $T_{CMB} = 3440$ K and would reduce conductivities to 2.2, 4.4 and 8.9 W/m/K.

Table 1
Parameters and dimensional scales for our thermochemical mantle convection model.

Parameter	Symbol	Value	Units	Non-dimensional
Governing parameters				
Reference Rayleigh number	Ra			3.0×10^8
Surface dissipation number	Di_{Surf}			1.2
Total internal heating	H	5.44×10^{-12}	(W kg^{-1})	20
Compositional heating ratio	dH_{prim}			1 – 20
Compositional parameters				
Buoyancy ratio	B			0.15 – 0.4
Volume fraction of dense material (%)	X_{prim}			3%
Thickness of initial dense layer	h_{DL}			0.05514
Physical & thermodynamical parameters				
Acceleration of gravity	g	9.81	(m s^{-2})	1
Mantle thickness	D	2891	(km)	1
Reference adiabat	T_{AS}	1600	(K)	0.64
Super-adiabatic temperature difference	ΔT_S	2500	(K)	1
Surface density	ρ_{Surf}	3300	(kg m^{-3})	1
Surface thermal expansion	α_{Surf}	5.0×10^{-5}	(K^{-1})	1
Surface thermal diffusivity	κ_{Surf}	7.5×10^{-7}	(m^2 s^{-1})	1
Heat capacity	C_P	1200	(J kg^{-1} K^{-1})	1
Surface conductivity	k_{Surf}	3	(W m^{-1} K^{-1})	1
Surface Grüneisen parameter	γ_{Surf}			1.091
Density jump at z = 660 km	$\Delta\rho_{660}$	400	(kg m^{-3})	0.1212
Clapeyron slope at z = 660 km	Γ_{660}	-2.5	(MPa K^{-1})	-0.0668
Surface temperature	T_{Surf}	300	(K)	0.12
CMB temperature	T_{CMB}	3440	(K)	1.376
Density jump at CMB	$\Delta\rho_{CMB}$	5280	(kg m^{-3})	1.6
Conductivity Parameters				
Depth- dependence contrast	K_D			2.5 - 10.0
Temperature- dependence exponent	n			0.0, 0.5, 0.8
Compositional correction	K_C			0.8
Viscosity Law				
Reference viscosity	η_{ref}	4.346×10^{20}	Pa · s	1
Viscosity ratio at z = 660 km	$\Delta\eta_{660}$			30
Logarithmic thermal viscosity ratio	$E_a(=\log(\Delta\eta_T))$			16.118
Logarithmic vertical viscosity ratio	$V_a(=\log(\Delta\eta_D))$			2.3026
Compositional viscosity ratio	$\Delta\eta_C$			30
Surface yield stress	σ_0	290	(MPa)	7.5×10^6
Yield stress gradient	$\dot{\sigma}_z$	0.01	(Pa Pa^{-1})	0.01

Fig. 2 summarizes primordial reservoir evolution for a few cases. The value for $(d\rho/\rho)_{prim}$ is calculated only for the primordial material field. The density of the primordial material field is compared with the mean density profile for the entire mantle layer. Thus, for the first 1 Gyr of evolution, when the primordial material is undisturbed, $(d\rho/\rho)_{prim} = 0$ because the mean density profile is identical to the density of the initial layer; absence of an anomaly is indicated by a soft white. Above this initial layer thickness, there is no primordial material and hence blank. For systems evolving with a canonical conductivity profile ($K_D = 2.5$), panels (a)-(c) highlight that a decreasing B is a first-order effect that destabilizes primordial reservoirs. For $B = 0.23$, a two-pile configuration for primordial reservoirs can remain stable over long geologic timescales (Figure S3, case #3). Because the initial temperature field is radially symmetric with random perturbations, pile configuration is dynamically generated and simulations do not impose a forcing towards a two-pile configuration. Jarvis et al. (1995) show that, in 2D spherical annulus geometry, the downwelling flow geometry can tend towards a degree-2 planform when the core-to-surface radii ratio (i.e., the curvature factor of the sphere) is Earth-like (~ 0.5). Thus, a two-pile configuration may be easier to establish in a 2D geometry. The density anomaly timeseries show that piles attain a mean anomaly of 1%, while the lighter material above has a negative anomaly relative to the adjacent, much denser, downwelling structures. Field snapshots show piles envelop a region with a positive RMS temperature anomaly of ~ 300 K and density anomaly < 1%. Furthermore, we observe a thin, dense layer with a density anomaly > 1% at the base and margins of the piles, consistent with tomographic models. In general, the average temperature increases by approximately 1000 K but remains under 4000 K (Figure S2, panels (a)-(c)).

By contrast, for $B = 0.15$, piles attain a mean density anomaly < 1%. Field snapshots show that a thin, dense anomaly > 1% may be present at the base of the piles (Figure S3, case #1). However, the primordial reservoirs are lighter and cannot overcome thermal buoyancy. Rapid entrainment of primordial reservoirs occurs as early as $t = 3.5$ Gyr, and piles become fully entrained by the end of the simulation. Due to entrainment, buoyant primordial material cools and spreads below the upper mantle, resulting in medium-sized suspended chemical heterogeneities above the piles. By the end of the simulation, the system attains a homogeneous distribution, and the horizontal average of density anomalies shrinks to zero.

Panels (c)-(e), with $B = 0.15$, highlight the stabilizing effect of an increasing bottom-to-top conductivity ratio on primordial reservoirs' evolution. Greater lower mantle thermal conductivity promotes cooler piles that are sufficiently dense to overcome thermal buoyancy. Even for buoyancy ratios that guarantee complete entrainment, greater lowermost mantle conductivity stabilizes piles and can preserve primordial reservoirs over large geologic timescales. This stabilizing effect is consistent with the findings of Guerrero et al. (2023). Because the onset of thermal instability is delayed only marginally compared to an increasing buoyancy ratio with a fixed conductivity profile, we argue that the bottom-to-top conductivity ratio is a secondary controlling parameter on the stability of primordial reservoirs.

Table 2
Averaged properties for all cases presented. Except for $t_{inst.}$, all values are averaged out over the time range 4-5 Gyr.

Case	B	dH_{prim}	K_D	K_C	n	⟨T⟩ (K)	$\langle T_{prim} \rangle$ (K)	global rms dT_{prim} (K)	negative rms dT_{prim} (K)	positive rms dT_{prim} (K)	h_C	Q_{Surf} (TW)	Q_{CMB} (TW)	Q_{vol}/Q_{Surf}	$\langle H_C \rangle$	$\langle A_{prim,CMB} \rangle$	$d\rho_{prim}/\rho$ (%)	min	max	global	−rms	+rms	$t_{inst.}$
1	0.15	10	2.5	1	0	2210	3470	680	1020	430	940	32.4	8.4	0.662	880	23	0.59	-2.04	4.12	0.44	0.43	0.45	3.6
2	0.19	10	2.5	1	0	2210	3830	380	290	480	1040	31.2	6.3	0.687	270	36	0.80	-0.21	1.43	0.35	0.39	0.32	5.1
3	0.23	10	2.5	1	0	2200	3690	290	240	340	780	30.2	4.7	0.711	190	52	1.15	0.38	1.76	0.22	0.23	0.20	9.2
4	0.15	10	5	1	0	2260	3640	220	190	250	600	33.4	10.6	0.641	260	35	0.66	0.14	1.14	0.24	0.23	0.24	4.3
5	0.15	10	10	1	0	2310	3470	120	120	120	270	37.6	15.3	0.571	240	37	0.84	0.44	1.14	0.14	0.14	0.14	5.6
6	0.15	1	9.185	0.8	0.5	2420	3300	110	140	90	140	26.9	5.3	0.796	180	60	0.83	0.36	1.35	0.16	0.14	0.19	12.0
7	0.15	1	9.185	0.8	0.8	2510	3340	110	130	80	160	23.2	2.6	0.925	140	73	0.67	0.19	1.36	0.19	0.16	0.25	12.0
8	0.15	5	9.185	0.8	0.5	2420	3550	200	170	230	510	26.8	4.3	0.800	180	59	0.69	0.29	1.19	0.16	0.16	0.17	8.8
9	0.15	5	9.185	0.8	0.8	2490	3730	330	260	420	810	22.4	2.1	0.956	180	62	0.56	0.02	1.15	0.22	0.25	0.20	6.9
10	0.15	10	9.185	0.8	0.5	2400	3860	440	420	450	900	27.6	6.6	0.777	740	26	0.52	-1.54	1.74	0.41	0.37	0.44	3.9
11	0.15	10	9.185	0.8	0.8	2500	3700	490	420	570	1240	23.0	3.4	0.931	1180	39	0.64	-2.71	2.22	0.47	0.60	0.37	3.4
12	0.19	1	9.185	0.8	0.5	2420	3300	110	130	90	130	26.3	5.7	0.817	160	57	1.06	0.60	1.84	0.19	0.14	0.29	12.0
13	0.19	1	9.185	0.8	0.8	2500	3360	90	120	70	120	23.5	3.1	0.912	160	62	1.00	0.54	1.80	0.21	0.17	0.29	12.0
14	0.19	5	9.185	0.8	0.5	2400	3490	170	160	180	450	26.0	3.8	0.825	150	62	0.90	0.52	1.64	0.20	0.16	0.27	12.0
15	0.19	5	9.185	0.8	0.8	2480	3610	230	200	260	570	22.9	1.2	0.935	140	81	0.75	0.12	1.59	0.27	0.24	0.30	9.7
16	0.19	10	9.185	0.8	0.5	2380	3830	340	270	420	920	25.8	4.6	0.831	210	43	0.87	0.16	1.48	0.27	0.32	0.24	6.7
17	0.19	10	9.185	0.8	0.8	2480	4190	540	480	610	1200	22.3	3.2	0.962	510	39	0.50	-1.50	1.50	0.61	0.74	0.55	4.7
18	0.19	15	9.185	0.8	0.5	2370	3910	480	380	590	1290	28.1	5.2	0.764	560	36	0.85	-1.70	2.19	0.39	0.47	0.34	3.7
19	0.19	15	9.185	0.8	0.8	2480	4060	670	580	760	1500	23.8	4.1	0.900	1210	26	0.76	-1.92	2.91	0.55	0.56	0.53	3.4
20	0.23	1	9.185	0.8	0.5	2410	3280	120	140	100	160	26.3	4.4	0.816	130	82	1.15	0.13	2.29	0.45	0.43	0.48	12.0
21	0.23	1	9.185	0.8	0.8	2490	3330	110	130	80	140	23.8	3.1	0.901	140	64	1.19	0.67	2.27	0.29	0.21	0.42	12.0
22	0.23	5	9.185	0.8	0.5	2410	3540	150	140	160	370	26.5	4.5	0.810	160	51	1.21	0.80	2.07	0.22	0.18	0.26	12.0
23	0.23	5	9.185	0.8	0.8	2470	3630	240	190	290	630	22.9	1.7	0.938	140	72	0.97	0.40	2.01	0.32	0.26	0.42	12.0
24	0.23	10	9.185	0.8	0.5	2370	3690	270	210	330	780	26.5	4.1	0.810	170	59	1.13	0.54	1.94	0.23	0.22	0.26	11.1
25	0.23	10	9.185	0.8	0.8	2470	4190	520	470	570	1130	23.5	1.9	0.912	210	46	0.97	0.22	1.74	0.34	0.36	0.33	6.6
26	0.23	15	9.185	0.8	0.5	2360	3950	500	390	630	1480	26.6	3.0	0.805	190	54	1.02	0.23	1.79	0.32	0.35	0.28	5.8
27	0.23	15	9.185	0.8	0.8	2450	4380	760	660	860	1690	21.4	1.6	1.003	500	50	0.70	-1.67	1.86	0.63	0.74	0.57	4.3
28	0.23	20	9.185	0.8	0.5	2350	4160	650	480	850	1790	26.7	4.5	0.804	350	39	0.96	-0.51	1.87	0.48	0.58	0.42	4.3
29	0.23	20	9.185	0.8	0.8	2440	4480	780	740	810	1570	21.3	2.1	1.007	580	49	0.72	-1.61	2.16	0.59	0.63	0.56	3.9
30	0.27	5	9.185	0.8	0.8	2460	3590	220	190	260	590	23.2	0.8	0.925	130	89	1.13	-0.05	2.48	0.51	0.51	0.52	12.0
31	0.27	10	9.185	0.8	0.5	2370	3620	230	190	280	660	25.0	2.6	0.857	140	63	1.28	0.69	2.38	0.33	0.26	0.46	12.0
32	0.27	10	9.185	0.8	0.8	2470	4090	480	430	530	1070	22.8	0.8	0.939	170	55	1.24	0.56	2.18	0.31	0.32	0.31	7.3
33	0.27	15	9.185	0.8	0.5	2360	3940	420	340	500	1050	26.4	3.6	0.812	180	49	1.32	0.52	2.16	0.31	0.35	0.28	8.8
34	0.27	15	9.185	0.8	0.8	2440	4380	640	560	730	1720	22.5	1.1	0.952	190	50	1.12	0.09	2.10	0.40	0.45	0.37	5.4
35	0.27	20	9.185	0.8	0.5	2350	4180	580	470	700	1450	26.7	3.3	0.804	190	46	1.22	0.28	2.05	0.39	0.46	0.34	6.7
36	0.27	20	9.185	0.8	0.8	2420	4390	750	650	860	2070	22.2	0.8	0.966	240	61	1.02	-0.89	2.13	0.45	0.48	0.43	4.7
37	0.31	10	9.185	0.8	0.5	2360	3570	190	160	230	550	24.9	2.3	0.863	130	70	1.41	0.69	2.94	0.45	0.34	0.64	12.0
38	0.31	10	9.185	0.8	0.8	2460	3980	420	370	480	940	21.8	0.0	0.984	140	67	1.38	0.70	2.69	0.40	0.33	0.52	9.7
39	0.31	15	9.185	0.8	0.5	2350	3860	340	300	390	820	26.0	3.0	0.825	160	54	1.57	0.89	2.65	0.31	0.29	0.34	12.0
40	0.31	15	9.185	0.8	0.8	2440	4430	620	610	630	1360	21.9	0.3	0.980	170	54	1.33	0.44	2.53	0.39	0.39	0.39	8.2
41	0.31	20	9.185	0.8	0.5	2330	3980	440	360	540	1140	26.8	2.6	0.799	160	54	1.50	0.68	2.54	0.35	0.36	0.34	9.6
42	0.31	20	9.185	0.8	0.8	2420	4350	720	630	820	1910	21.7	-0.3	0.988	160	68	1.23	0.27	2.48	0.43	0.40	0.47	5.6
43	0.35	10	9.185	0.8	0.8	2450	3860	370	330	410	860	21.9	-0.1	0.981	120	75	1.43	0.57	3.17	0.50	0.41	0.65	12.0
44	0.35	15	9.185	0.8	0.8	2430	4260	620	590	640	1360	22.5	-0.1	0.952	160	67	1.59	0.72	2.98	0.41	0.35	0.49	7.5
45	0.35	20	9.185	0.8	0.5	2330	3870	360	300	420	930	25.5	2.0	0.842	140	60	1.66	0.91	3.12	0.40	0.31	0.55	12.0
46	0.35	20	9.185	0.8	0.8	2410	4260	670	570	770	1810	20.8	-1.5	1.032	140	78	1.36	0.30	2.87	0.51	0.45	0.60	6.7
47	0.4	10	9.185	0.8	0.8	2440	3850	360	330	390	810	21.9	-0.1	0.980	120	77	1.70	0.61	3.75	0.59	0.50	0.74	12.0
48	0.4	15	9.185	0.8	0.8	2420	4130	560	510	600	1210	22.4	-0.4	0.956	140	73	1.78	0.67	3.47	0.55	0.49	0.63	9.7
49	0.4	20	9.185	0.8	0.5	2320	3800	320	280	360	890	24.9	0.3	0.861	130	74	1.89	0.85	3.70	0.54	0.45	0.67	12.0
50	0.4	20	9.185	0.8	0.8	2390	4060	570	460	710	1480	21.8	-2.2	0.983	120	88	1.43	-0.03	3.58	0.77	0.70	0.88	8.4
51	0.23	10	9.185	0.8	0.5	2630	4590	710	690	740	1300	40.1	4.7	0.744	410	32	0.79	-0.69	3.20	0.63	0.62	0.64	4.87
52	0.23	10	9.185	0.8	0.8	2830	4450	760	640	890	1940	34.0	2.8	0.868	1110	25	1.19	-1.79	4.98	0.59	0.64	0.55	2.92

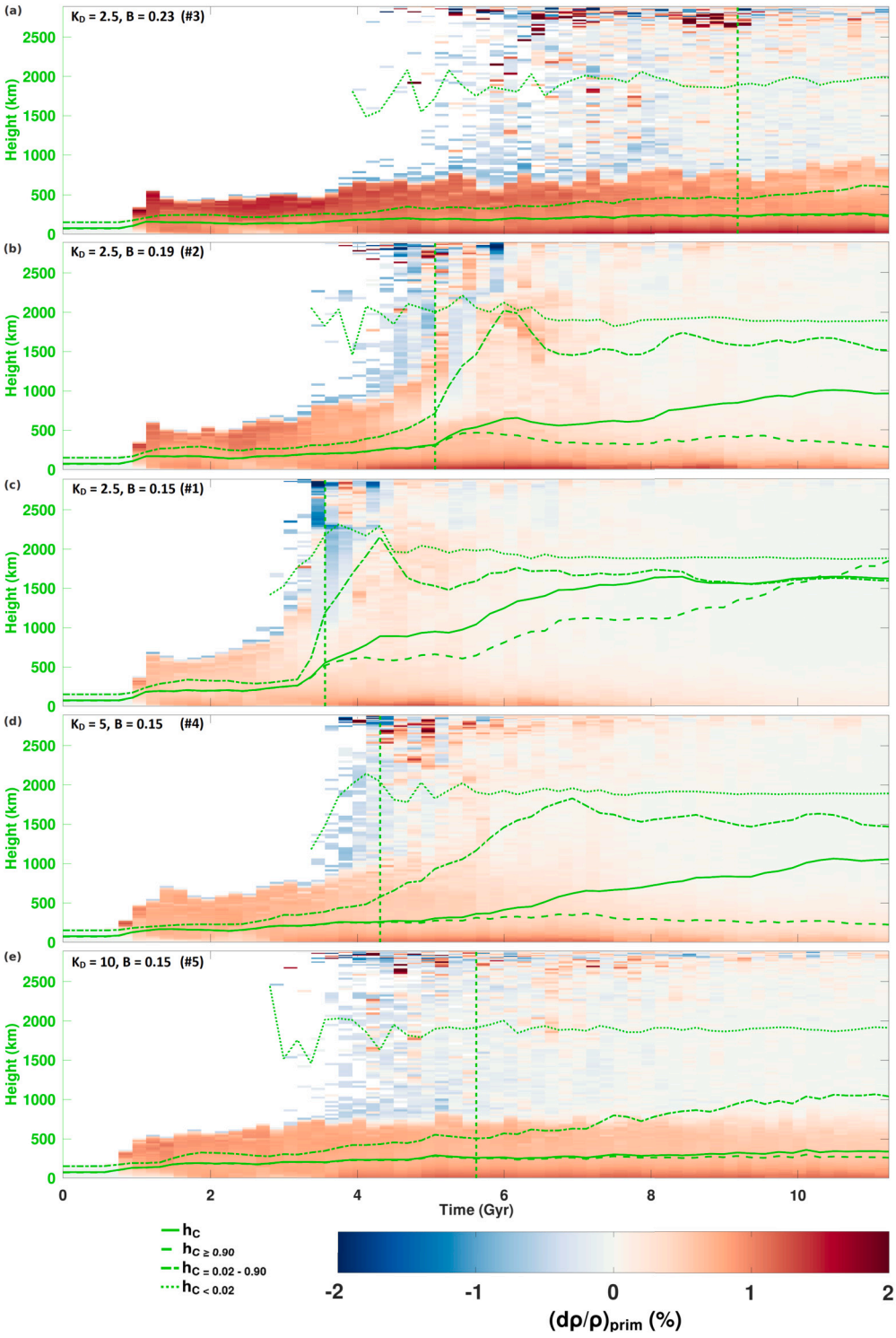

Fig. 2. Evolution of the horizontally averaged primordial material density anomalies is illustrated for cases featuring a decreasing B for $K_D = 2.5$ ((a) - (c)) and an increasing K_D for $B = 0.15$ ((c) - (e)). Mean height of primordial material is plotted on top of the density anomaly time series. The dashed-green vertical line indicates the onset of instability in thermochemical reservoirs. Temperature timeseries of primordial material is shown in Figure S2. The field snapshots for density anomalies are shown in Figure S3.

Prior to the onset of thermal instability, the difference between mean and maximum pile temperatures steadily increased. Additionally, the maximum temperature of upwelling primordial material is greater for a larger buoyancy ratio. This finding is consistent with the fact that hotter internal temperatures are required to overcome downward chemical buoyancy. The minimum pile temperature drops significantly because the primordial material from upwellings rapidly cools below the upper mantle. The piles maintain a smaller temperature variation for simulations with a greater conductivity (Figure S2). Thus, greater conductivity regulates pile temperatures and ensures that thermal buoyancy does not overcome chemical buoyancy.

The mineral physics-derived depth-dependent profile takes on values upwards of 30 W/m/K towards the CMB (e.g., Deschamps and Hsieh (2019)), consistent with K_D around 10. The depth-dependence of lower

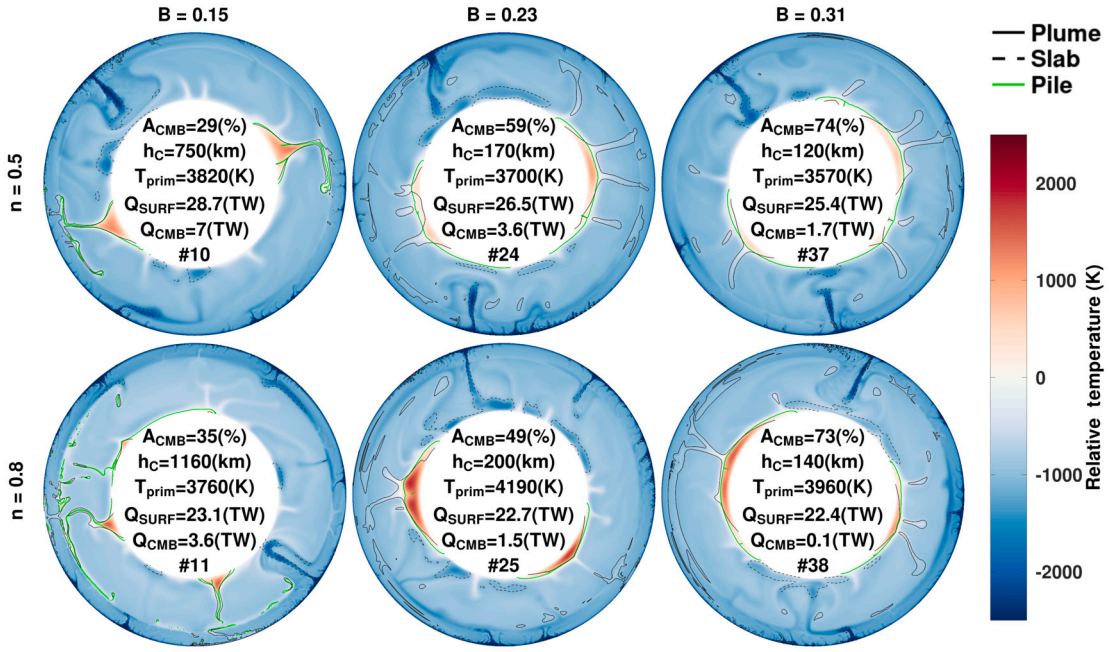

Fig. 3. Temperature fields relative to CMB temperature ($T - T_{CMB}$) at $t = 4.5$ Gyr are illustrated for cases featuring $n = 0.5$ and 0.8 and $B = 0.15$ (left column), 0.23 (center column), and 0.31 (right column). Heat-producing element enrichment is fixed at $dH_{prim} = 10$ for all cases presented. Plumes are indicated by a solid black contour, slabs are indicated by a dashed black contour, and piles are indicated by a solid green contour. Relative temperature corresponds to the values indicated on the colorbar. The corresponding thermal conductivity and primordial density anomaly fields are shown in Figures S4 and S5.

mantle mineral conductivity has a stabilizing effect on piles, allowing them to be composed of material with relatively low chemical density contrast. For the remainder of this study, the mineral physics-derived depth-dependence (given in Equation (1)), with bottom-to-top conductivity ratio equivalent to a linear increase $K_D \sim 9$, is employed.

3.2. Buoyancy ratio and temperature-dependent conductivity

Fig. 3 shows the relative temperature field at $t = 4.5$ Gyr for cases featuring variable temperature-dependent conductivity with $n = 0.5$ or 0.8 and different buoyancy ratios. For our reference buoyancy ratio $B = 0.23$, the piles' mean temperature and topography increase for greater n. Consequently, piles' CMB coverage decreases. Approximately half of the CMB surface is covered, which is greater than the observed CMB coverage by LLSVPs on the Earth, and hotter pile temperatures result in negative density anomalies. Our modeled piles are characterized by a core of material with $d\rho/\rho < 1\%$ and surrounded by a thick, dense exterior with $d\rho/\rho > 1\%$ (Figure S5). For $n = 0.8$, the less dense regions within the piles take on a more bumpy topography consistent with the plume structures surrounding them.

The lighter reservoirs (lower B) are more susceptible to being pooled by denser downwelling currents. Pile topography is taller than cases with higher B, and the CMB coverage is comparable to observations of LLSVPs in the Earth's mantle. Bulk entrained material in plume conduits attains a negative density anomaly resulting from their low intrinsic density contrast in combination with high temperature relative to the ambient mantle. The remaining material in a pile attains $d\rho/\rho < 1\%$, which overlies a thin, dense layer with $d\rho/\rho > 1\%$ atop the CMB (Figure S5).

The heavier reservoirs (higher B) are less susceptible to lateral advection by downwelling currents. The piles now take on a much flatter morphology, and their lateral extent tapers off slowly, resulting in a CMB coverage exceeding that observed for Earth's LLSVPs. At the top of the piles, $d\rho/\rho$ is larger because the primordial material is denser than the adjacent cold downwelling material (Figure S5). Piles' interiors are less dense, and the density reduction and volume depend on the piles' conductivity and temperature. Because of these dependencies, the volume of this region marginally increases with time due to the constant internal heating conditions we adopt.

Due to the constant internal heating, the bulk core of the piles attains greater mean and maximum temperatures, and the pile height is increased (consistent with the findings of Li et al. (2022) and Guerrero et al. (2023)). Furthermore, because the piles are poorly conducting compared to the ambient mantle (Figure S4), the positive temperature anomaly grows and contributes to their thermal buoyancy. The degree to which this temperature anomaly influences reservoir stability depends primarily on chemical buoyancy and secondarily on the piles' ability to evacuate heat.

For moderate temperature-dependence ($n = 0.5$) and $B = 0.15$, the onset of thermal instability occurs by approximately 4 Gyr and the piles are effectively entrained by the end of the simulation, leaving only two tiny remnant piles (Figures S6 and S8, #10). For $B = 0.23$, thermal instability only occurs after 11 Gyr and primordial reservoirs attain an antipodal two-pile configuration (Figures S6 and S8, #24). For $B = 0.31$, primordial reservoirs remain stable and accumulate into one large pile (Figures S6 and S8, #37).

For stronger temperature-dependent conductivity ($n = 0.8$), HPE-enriched piles' conductivity decreases further so that excess heat easily accumulates and pile topography increases. For $B = 0.15$, the onset of thermal instability occurs by approximately 3.5 Gyr and piles are effectively entrained by the end of the simulation (Figures S7 and S9, #11). For $B = 0.23$, thermal instability occurs at approximately 6.5 Gyr, and primordial reservoirs attain a single pile configuration towards the end of the simulation (Figures S7 and S9, #25). For $B = 0.31$, primordial reservoirs accumulate into one large pile by 9 Gyr, and the thermal instability occurs at approximately 10 Gyr (Figures S7 and S9, #38) In summary, greater n decreases stability, meaning that for conductivity values found in experiments, relatively heavy material (with $\sim$ 4% iron excess and ~140-150 kg/m^3 density excess) may lead to structures resembling a bundle-like structure (Davaille and Romanowicz, 2020), rather than homogeneous piles.

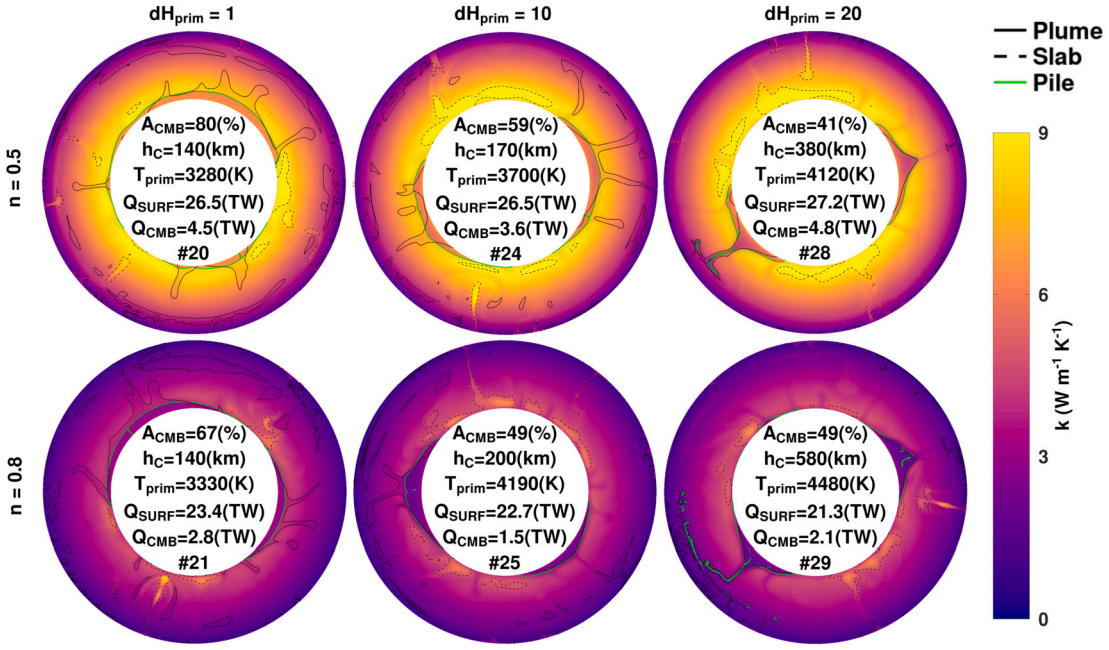

Fig. 4. Conductivity field snapshots at $t = 4.5$ Gyr are illustrated for cases featuring $n = 0.5$ and 0.8 and $dH_{prim} = 1$ (left column), 10 (center column), and 20 (right column). Buoyancy ratio is fixed at $B = 0.23$ for all cases presented. Plumes are indicated by a solid black contour, slabs are indicated by a dashed black contour, and piles are indicated by a solid green contour. Conductivity corresponds to the values indicated on the colorbar. The corresponding relative temperature and primordial density anomaly fields are shown in Figures S10 and S11.

3.3. Heat-producing element enrichment and temperature-dependent conductivity

Fig. 4 shows snapshots of the conductivity field at $t = 4.5$ Gyr for cases featuring variable temperature-dependent conductivity, $B = 0.23$, and different HPE enrichment (dH_{prim}). Without HPE enrichment ($dH_{prim} = 1$), piles remain relatively flat and cover a significant fraction of the CMB. The piles' conductivity is comparable to the adjacent ambient mantle, which helps regulate their temperature. The topography of piles then increases with increasing dH_{prim}. However, it is less pronounced than the increase obtained by a decrease in B. Outside piles, the conductivity and temperature fields remain relatively unchanged with increasing dH_{prim} (regardless of n). Because of the greater rate of heat production, piles accumulate heat rapidly, leading to larger temperature excess (Figure S10). Consequently, the conductivity reduction is also larger, reducing heat transfer towards the regular mantle and helping piles remain hot.

For cases with $n = 0.5$, the conductivity field in the lower mantle outside piles is comparable to that obtained for $K_D \sim 2.5$. The conductivity field within piles is lower than in the surrounding ambient mantle, and the conductivity within the region of the positive temperature anomaly maintains values > 3 W/m/K (the surface conductivity value, k_{Surf}). For cases with $n = 0.8$, the lower mantle conductivity field is comparable to k_{Surf} (i.e., $K_D \sim 1$), and conductivity takes on values $< k_{Surf}$ within piles.

Interestingly, for either conductivity model, the part of the CMB covered with piles attains a thin layer of marginally more conductive material because the bottom of the piles remains cooler compared with the temperature anomaly above it. Due to large temperature anomalies caused by HPE enrichment, the thermal gradient at the base becomes locally or regionally negative. When the temperature-dependent conductivity is stronger, the magnitude of negative heat flux is smaller for a similar temperature anomaly within the pile. When HPE enrichment is absent, heat flow remains positive due to the marginally cooler base of the pile relative to the core-mantle boundary. However, the magnitude is so low that it effectively insulates the core-mantle boundary. Thus, piles enriched in HPEs may lose heat more efficiently to the core at the CMB than to the ambient mantle at their top side.

Regardless of the temperature dependence, for $dH_{prim} = 1$, piles remain stable throughout the simulation and maintain a relatively flat morphology with high core-mantle boundary coverage. The pile tops attain a greater $d\rho/\rho$ than their base for the buoyancy ratio tested. The pile lower layer remains denser than its surroundings, but $d\rho/\rho$ is now $< 1\%$. Piles' temperature is greater for greater dH_{prim}, and their interiors have lower $d\rho/\rho$ and may even be less dense than the ambient mantle. For $dH_{prim} = 20$, a thin, dense layer partially covering the core-mantle boundary is still possible. Pile instability occurs at approximately $t = 4$ Gyr for both conductivity models as primordial material is ejected or lifted away in a thin plume conduit (Figure S12). When pile conductivity is more sensitive to temperature, the density anomaly may take on a more plume-like morphology, consistent with tomographic models reported by (French and Romanowicz, 2014).

4. Discussion

4.1. Chemical density contrast and enrichment in heat-producing element: general trends

Fig. 5(a) plots the time for the onset of thermal instability, $t_{inst.}$, corresponding to the instance at which primordial material with concentration $< 90\%$ achieves rapid uplift relative to material with concentration $\geq 90\%$, in the B-dH_{prim} parameter space. We consider a case as fully stable if $t_{inst.} > 10$ Gyr. Overall, B and dH_{prim} influence primordial reservoir evolution more strongly for greater n. For $n = 0.5$, the boundary for fully stable cases follows a linearly increasing monotonic trend in B and dH_{prim}. For $n = 0.8$ and $dH_{prim} < 10$, the instability boundary coincides with the $n = 0.5$ cases. However, when $dH_{prim} = 10$, B needs to be > 0.27 (corresponding to $(d\rho/\rho) \sim 3.44\%$) to maintain stability during the entire simulation. For greater dH_{prim}, even cases with $B = 0.4$ (i.e., $(d\rho/\rho) \sim 5\%$) become unstable within the run duration.

Figs. 5(b) and 5(c), plotting the mean density anomalies and the mean height of piles at $t = 4.5$ Gyr for each case presented in Fig. 5(a), show that given B and dH_{prim}, density anomalies are smaller when

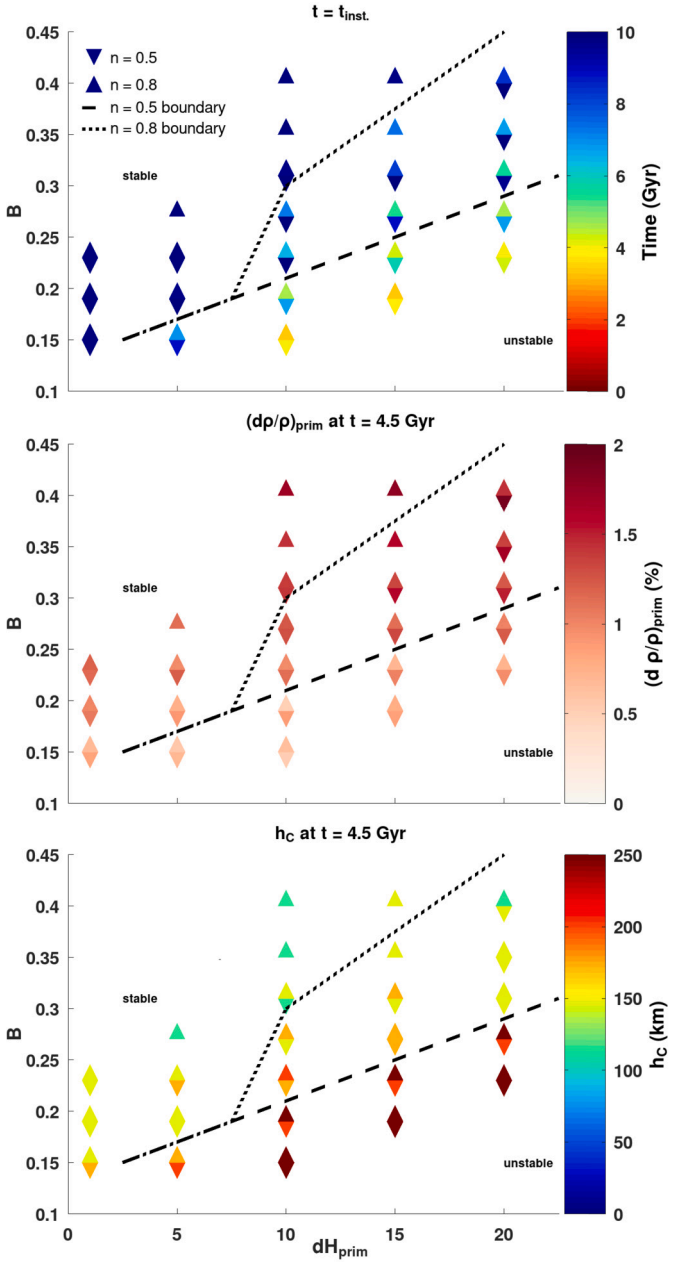

Fig. 5. Primordial reservoir stability regime diagram indicating the onset of thermal instability, $t_{inst.}$, mean density anomaly ($(d\rho/\rho)_{prim}$), and mean height of piles (h_C) in $B - dH_{prim}$ parameter space for all cases featuring K_{DH} and $K_C = 0.8$ with constant heating conditions.

thermal conductivity has a greater temperature dependence. This finding is consistent with poorly conducting piles becoming hotter (and therefore less dense and taller) compared to more conductive piles. Combined with the effect of temperature on density, piles attain a much smaller effective density contrast relative to their intrinsic chemical density contrast. Nevertheless, the effective density contrast ($(d\rho/\rho)_{prim}$) is greater with greater intrinsic (or chemical) density contrast. The density anomalies for unstable cases are $\lessapprox 1\%$ when $n = 0.5$, but are between 1 and 2% when $n = 0.8$. Overall, the density anomalies of piles remain positive and are limited to a few percent relative to the ambient mantle. Density anomalies $\gtrapprox 1\%$ characterize stable piles for all examined heating conditions. However, considering stronger temperature-dependent thermal conductivity, a greater density anomaly does not necessarily guarantee pile stability. Interestingly, density anomalies for stable piles are consistent with the range of values inferred from various tomographic models (e.g., Trampert et al., 2004; Lau et al., 2017; Davaille and Romanowicz, 2020).

4.2. Perspectives on lower mantle conductivities

From the regime plot (Fig. 5), it is clear that temperature-dependent conductivity plays a decisive factor in the fate of primordial reservoirs when HPE enrichment is present. If piles cannot evacuate this internal heat efficiently (e.g. because their conductivity is poor), the growing temperature anomaly results in an ejection of hot and highly concentrated primordial material. Thus, measurements of mantle materials and their respective parametrized conductivity models can significantly affect the evolution of the lowermost mantle thermochemical structure.

Currently, conductivity measurements for pyrolite at both high temperatures and pressures sparsely sample the lower mantle (Geballe et al., 2020). Moreover, constraints on the various dependencies of thermal conductivity (i.e., pressure, temperature, and composition) are based on parametrizations of measurements made with non-simultaneous high temperature and pressure conditions (e.g., Hsieh et al., 2017, 2018; Zhang et al., 2023). As such, consensus on the strength of the mantle conductivity's temperature-dependence has not yet been reached. In our calculations, we used two temperature-dependent thermal conductivity strengths that result in pyrolytic lower mantle conductivities that overlap the upper and lower bounds of measurements reported by Geballe et al. (2020). The mean pyrolytic lowermost mantle conductivity is ~ 9 and ~ 5 W/m/K for $n = 0.5$ and 0.8, respectively. The corresponding conductivities for piles are sensitive to temperature (and hence HPE enrichment). In general, piles in the lowermost mantle attain mean values of ~ 6 and ~ 2.5 W/m/K for $n = 0.5$ and 0.8, respectively. The differing evolution of primordial reservoirs revealed by this study suggests that new measurement efforts should focus on deriving the temperature dependences of lowermost mantle minerals at high pressure and a more detailed exploration of lower mantle conductivities at both high temperature and high pressure.

For mantle materials (non-metallic minerals), total thermal conductivity is the sum of lattice (k_{latt}) and radiative (k_{rad}) components. However, while temperature dependence in k_{latt} decreases its magnitude with increasing temperature, k_{rad} increases. Estimates of k_{rad} based on samples of bridgmanite ranged from below $\sim$ 0.5 (Goncharov et al., 2008) up to $\sim$ 5 W/m/K (Keppler et al., 2008; Goncharov et al., 2015). Current estimates based on single crystal bridgmanite place k_{rad} between 2 and 5 W/m/K, corresponding to temperatures between 3000 and 4500 K at CMB pressures (Murakami et al., 2022). Based on measurements by Murakami et al. (2022) and a T_{CMB} of 3500 K, we estimate a total conductivity of 9.7 W/m/K for k_{latt} with n = 0.5 and 6.3 W/m/K with n = 0.8. A system evolving solely with k_{latt} promotes significant temperature anomalies (and lower k_{latt}) within piles, so including k_{rad} will mitigate the positive feedback loop, and the piles' mean temperature can settle at a different value. Because the temperature effect in k_{latt} is dominant and the total conductivity (including k_{rad}) is comparable to the values we obtain in our calculations, we chose to neglect this effect. Nevertheless, the effect of radiative thermal conductivity on the stability of primordial reservoirs is not trivial, and the interplay with different heating enrichment scenarios requires further examination.

4.3. Perspectives on the density of LLSVPs

In order to keep with traditional views of LLSVPs, primordial reservoirs need to be characterized by high chemical density contrasts. Specifically, higher density contrasts prevent the entrainment and allow for dome-like piles to form, consistent with classic tomographic images. The piles' evolution is controlled by their effective density, which integrates both compositional and thermal effects. Because piles are hotter than the surrounding mantle, their effective density contrast is lower.

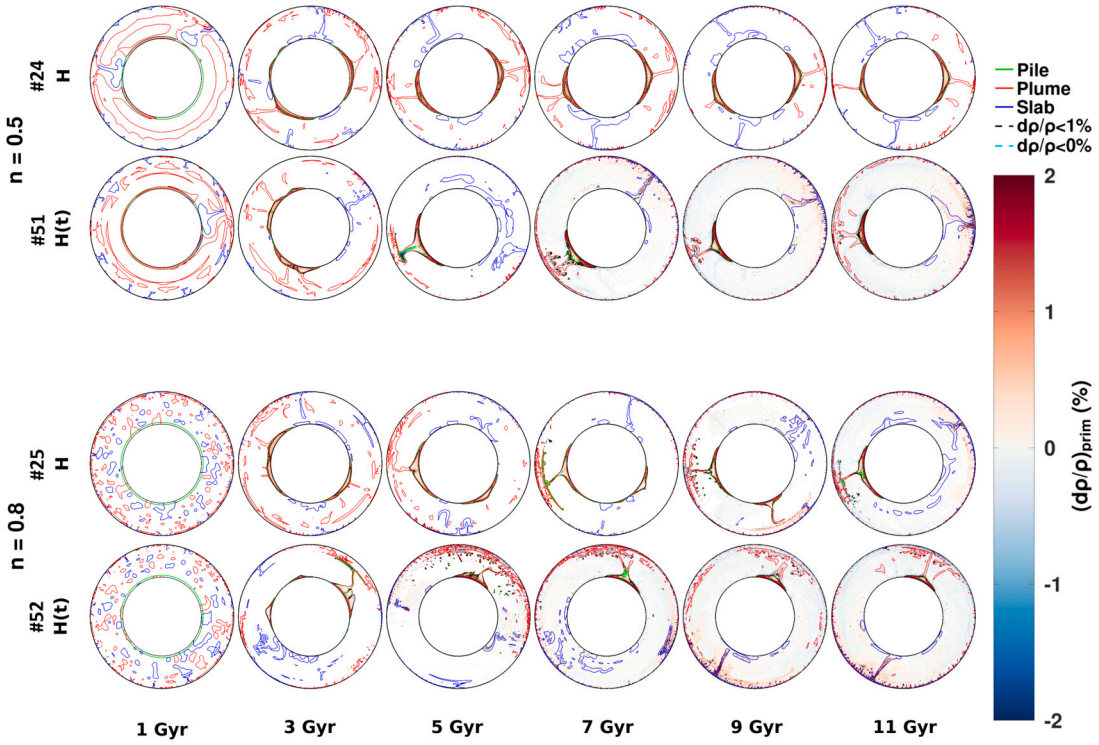

Fig. 6. Density anomalies for the primordial field are sampled at 2 Gyr intervals starting at 1 Gyr. These snapshots correspond to cases featuring constant and time-dependent internal heating for cases with $n = 0.5$ (#24 (first row) and #51 (second row)) and with $n = 0.8$ (#25 (third row) and #52 (fourth row)). In the snapshots, solid red contours indicate upwelling regions, solid blue contours indicate downwelling regions, solid green contours indicate primordial material with $C > 0.90$, dashed black contours enclose regions with density anomalies lesser than 1%, and dashed cyan contours enclose regions with density anomalies lesser than 0%.

The effective density contrast is thus sensitive to parameters controlling the piles' temperature. Therefore, the density excess that piles can attain is strongly affected by heat input from HPEs and piles' affinity for conducting this heat to the ambient mantle, which is controlled by thermal conductivity. Since conductivity decreases with increasing temperature, enrichment in HPE will likely have a durable impact on piles' evolution.

The range of B we employed implies an intrinsic chemical density contrast between 1.8 and 5.0% with respect to the reference density profile. Within the piles, the density structure varies for different intrinsic density contrasts, heat-producing element enrichment, and temperature-dependent conductivity. For cases featuring $dH_{prim} = 10$, the $(d\rho/\rho)_{prim}$ that the piles attain is between 0.5 and 2.0%, which encompasses the range of densities determined by seismology. For $B = 0.15$, the minimum chemical density contrast is $\sim -1.5\%$ and $\sim -2.7\%$ for moderate and strong n, and the fate of these piles tends to bulk entrainment of material. For larger B, the difference between the minimum density contrasts for weak and strong thermal conductivity models shrinks. For $B = 0.23$, the minimum density becomes strictly positive with values $\sim 0.5\%$ ($n = 0.5$) and $\sim 0.2\%$ ($n = 0.8$). However, the piles evolving with moderate temperature-dependence remain stable, whereas those with stronger temperature-dependence attain rapid material erosion by approximately 6 Gyr.

While chemical density contrast is the dominant controlling parameter on piles' evolution, thermal conductivity and heat input by HPEs strongly affect the overall density and, thus, piles' stability in the lower mantle. There is no agreement on the density of LLSVPs, but normal-mode and tidal tomography studies point to LLSVPs $\sim 1\%$ denser than the ambient mantle (e.g., Trampert et al., 2004; Lau et al., 2017). Our calculations reveal that if thermal conductivity strongly depends on temperature, even relatively high chemical density contrast may not lead to a dome-like structure but a less stable structure, analogous to the bundle-like morphology observed by (Davaille and Romanowicz, 2020). Conversely, to compensate for the high thermal contribution, the chemical contribution to density could also be larger than expected. Assuming that LLSVPs are enriched in iron, this would require iron content in excess of 4% relative to the ambient mantle, which is supported by joint inversion for seismic velocity and attenuation (Deschamps et al., 2019).

4.4. Perspectives on internal heating and heat-producing element enrichment in LLSVPs

Internal heating is a strong factor in the evolution of thermochemical piles. We applied constant heating conditions to examine the effects of heterogeneous thermal conductivity. For the cases presented, the base heating rate $H = 5.44 \times 10^{-12}$ W/kg is representative of present-day internal heating. For some cases with large buoyancy ratios, $t_{inst.}$ is often much longer than the typical aggregate half-life of heat-producing elements (i.e., $\sim$ 3.0 Gyr). Thus, a much greater initial internal heating rate is required to attain the present-day heating rate.

For cases with large dH_{prim}, earlier episodes of greater heat input could result in unstable piles. Fig. 6 illustrates the evolution of thermochemical piles with time-dependent heating conditions and physical parameters corresponding to cases #24 and #25. Time-dependent heating cases have an initial heating rate of $H = 15.4 \times 10^{-12}$ W/kg and a decay rate of 3.0 Gyr. Regardless of n, the dense material pools into a single pile by 5 Gyr. The thermal buoyancy effect dominates within the first 5 Gyr, and erosion is rapid. Internal heating wanes significantly after 5 Gyr, and its impact on pile configuration weakens. The precise effect of time-dependent heating is non-trivial and may alter conclusions made regarding combinations of B and dH_{prim} pairs for cases in the stable regime. The $t_{inst.}$ associated with each case may shift to earlier periods; however, the general conclusions regarding stability and heterogeneous thermal conductivity should still hold.

In numerical modeling, dH_{prim} is often an assigned value that falls within the range of possible heating scenarios. For instance, based on the volume and mass estimates of LLSVPs by Cottaar and Lekic (2016), Citron et al. (2020) place the potential range of dH_{prim} between 10 and 100. In practice, these model setups allow for systematically exploring trends and determining regime changes in dynamics. One caveat regarding an assigned enrichment value is that the total internal heating budget may exceed the values constrained by geodynamic, geochemical, or cosmochemical studies (Korenaga, 2008; Arevalo et al., 2009; Javoy et al., 2010; Gale et al., 2013; Turcotte and Schubert, 2014). Given a specific total heating rate and dH_{prim}, an appropriate proportion of internal heating for the ambient mantle can be derived. However, the enrichment in each radiogenic isotope in the aggregate material assumed by different models of internal heating budget varies significantly (Šrámek et al., 2013). Furthermore, enrichment factors are sensitive to the mass fraction of the LLSVPs relative to the entire mantle. Thus, a thin layer of LLSVPs material supports more HPEs than a thicker layer to maintain the mantle's internal heating rate heat budget. For example, layers with initial thicknesses of 150 and 300 km may attain a heating rate of approximately 70 and 30 times that of the ambient mantle, respectively. These heating rates are within the range of estimates for deep mantle reservoirs but are much larger than those implemented in simulations.

Given the work presented in this study, we should expect that primordial reservoirs that support higher heating enrichment should be more unstable and thus attain a smaller bulk mass and volume at present compared to their initial state. We conjecture that it may be possible for the LLSVPs region to have been larger in their early history (supporting a lower enrichment factor) and erode down to the size estimated by Cottaar and Lekic (2016). Studies on magma ocean crystallization may help constrain this layer's initial mass and volume and place limits on the enrichment factor. Studies, including radioactive decay and core cooling, may be required to assess whether these estimates can result in the piles we observe today.

5. Conclusions

We explored the dynamics and stability of thermochemical piles and discovered that their fate is determined by heterogeneous thermal conductivity, specifically by the strength of thermal conductivity's temperature dependence. First, we found that a purely depth-dependent bottom-to-top thermal conductivity contrast can stabilize thermochemical piles with a small density contrast and moderate enrichment in heat-producing elements. Next, for a fully heterogeneous thermal conductivity, we showed that for moderate HPE enrichment ($dH_{prim} = 10$), piles remain stable for $B \geq 0.23$ and moderate temperature dependence $n = 0.5$. Pile instability is initiated earlier for a stronger temperature-dependence ($n = 0.8$), but piles can remain stable for a sufficiently high B. Furthermore, for variable dH_{prim} and moderate buoyancy ($B = 0.23$), pile stability occurs for $dH_{prim} \leq 10$ with moderate temperature dependence ($n = 0.5$). A stronger temperature-dependent conductivity ($n = 0.8$) becomes unstable for $dH_{prim} \geq 10$. Piles remain stable for the entire simulation when HPE enrichment is absent. Overall, for both temperature-dependent conductivities considered, pile instability occurs for a combination of low B and high dH_{prim} that promotes the domination of thermal buoyancy over chemical buoyancy. When temperature-dependent conductivity is stronger, thermal buoyancy is intrinsically stronger. Thus, a greater chemical density contrast is required to maintain stable and long-lived piles. Given the dominant influence of HPE enrichment on piles' thermal conductivity, the fate of thermochemical piles and their retained present-day volume should also be re-examined in the context of time-dependent internal heating and estimated enrichment factor.

CRediT authorship contribution statement

J.M. Guerrero: Writing – review & editing, Writing – original draft, Visualization, Software, Investigation, Formal analysis, Conceptualization. **F. Deschamps:** Writing – review & editing, Writing – original draft, Supervision, Resources, Methodology, Investigation, Funding acquisition, Conceptualization. **Wen-Pin Hsieh:** Writing – review & editing, Resources, Methodology. **P.J. Tackley:** Writing – review & editing, Software.

Declaration of competing interest

The authors declare that they have no known competing financial interests or personal relationships that could have appeared to influence the work reported in this paper.

Data availability

Data will be made available on request.

Acknowledgements

This study was funded by the National Science and Technology Council grant NSTC 111-2116-M-001-029 and Academia Sinica grant AS-IA-108-M03. The authors thank the James Badro for handling our manuscript. The authors thank Allen McNamara and an anonymous reviewer for their constructive comments that helped improve the paper.

Appendix A. Thermochemical mantle convection

The non-dimensional governing equations for compressible thermochemical mantle convection with infinite Prandtl number are solved using the finite volume code StagYY (Tackley, 2008). The governing equations are summarized below: conservation of mass

$$\nabla \cdot (\rho \mathbf{v}) = 0, \tag{A.1}$$

conservation of momentum

$$\nabla \cdot \sigma - \nabla P = Ra(\rho \alpha T - BC)\hat{\mathbf{r}}, \tag{A.2}$$

conservation of energy

$$\rho C_P \frac{DT}{Dt} = -\mathrm{Di}_{Surf} \alpha \rho T v_r + \nabla \cdot (k \nabla T) + \rho H + \frac{\mathrm{Di}_{Surf}}{Ra} \sigma : \dot{\epsilon} \tag{A.3}$$

and conservation of composition

$$\frac{DC}{Dt} = 0. \tag{A.4}$$

The governing parameters include the Rayleigh number Ra, the dissipation number Di_{Surf}, the buoyancy ratio B, and the internal heating rate H. A detailed description of the buoyancy ratio and internal heating rate are discussed below. The variables include the velocity $\mathbf{v}$ (where v_r is the radial component), pressure P, composition C, and temperature T. The material properties include the density ρ, thermal expansivity α, heat capacity C_P, dynamic viscosity η, and the thermal conductivity k. The radial profiles for the reference state are included in Figure S1 of the supplemental material. The viscosity and thermal conductivity are dependent on depth, temperature, and composition and their variations are discussed in the supplemental material. The radial coordinate is given by r and the corresponding unit vector is given by $\hat{\mathbf{r}}$. σ is the deviatoric stress tensor (evaluated by $\eta\left(\nabla \mathbf{v} + \nabla \mathbf{v}^{\mathbf{T}} - \frac{2}{3}(\nabla \cdot \mathbf{v})\mathbf{I}\right)$ where $\mathbf{I}$ is the identity matrix) and $\dot{\epsilon}$ is the strain rate tensor and the viscous dissipation of heat is given by their double-dot product $\sigma : \dot{\epsilon}$.

Appendix B. Mantle internal heating and heat-producing element enrichment

In our simulations, the mantle is heated internally by the decay of heat-producing elements and at the bottom by the core. We consider constant heating conditions so that the effect of heterogeneous conductivity may be isolated under variable governing parameters. The total internal heating rate is controlled by a reference value, H, and accounts for the internal heating rates representative of regular mantle material and primordial material. We consider $H = 5.44 \times 10^{-12}$ W/kg, which represents a present-day internal heating rate for an aggregate of heat-producing elements. To account for the possible enrichment of heat-producing elements (HPEs) in primordial material (e.g., Richter, 1985; Kellogg et al., 1999), we adopt a compositional heating ratio (or enrichment factor), dH_{prim}, that expresses the internal heating rate of thermochemical piles relative to regular mantle material. The internal heating rate of regular mantle material, H_M, (outside of primordial material) is adjusted so that the average internal heating rate of the mantle remains equal to the specified reference value. This internal heating rate is given by

$$H_M = H \times \left(\frac{1 + C_{total}(dH_{prim} - 1)}{1 + \bar{C}(dH_{prim} - 1)} \right) \tag{B.1}$$

where C_{total} and $\bar{C}$ are the total amount and the average value of primordial material, respectively. When time-dependent heating is considered, we multiply Equation (B.1) by $\exp\left(\frac{t_{4.5} - t}{\tau_{1/2}} \log 2 \right)$ where $t_{4.5} = 4.5$ Gyr is time at present and $\tau_{1/2}$ is the half-life of radioactive decay. For time-dependent cases #51 and #52, we assume a decay rate with a half-life of $\tau_{1/2} = 3$ Gyr and the heating rate at the start of the simulation is approximately three times larger than in constant-heating cases.

Appendix C. Dynamic core-mantle boundary temperature

The heat flow from the core to the mantle is attributed to the thermal gradient at the bottom boundary determined by the core-mantle boundary temperature (i.e., $T_{CMB} = 3440$ K). When constant heating is considered, T_{CMB} is held fixed throughout the simulation. For time-dependent cases #51 and #52, T_{CMB} dynamically evolves according to the energy equation given by

$$\frac{4\pi}{3} R_{CMB}^3 \rho_c C_{p,c} \frac{dT_{CMB}}{dt} = -4\pi R_{CMB}^2 F_{CMB}. \tag{C.1}$$

where R_{CMB} is the core-mantle boundary radius, ρ_c is the liquid outer-core density, $C_{p,c}$ is the liquid outer-core heat capacity and F_{CMB} is the mean core-mantle boundary heat flux. We adopt a ρ_c value of 11000 kg/m^3 and $C_{p,c}$ value of 800 J/kg/K. Because the core temperature evolves due to the heat extracted at the core-mantle boundary, it is possible that beneath the hottest regions of the lowermost mantle heat may flow from the mantle to the core and thus raise the CMB temperature.

Appendix D. Thermochemical field

The thermochemical field distinguishes between regular mantle material and a chemically distinct, primordial, material. The primordial material we consider in our models characterizes chemically distinct heterogeneities at the base of the Earth's mantle as a result of early differentiation. The evolution of thermochemical reservoirs is modeled using the tracer ratio method (Tackley and King, 2003). The number of tracers per cell is 40 so that there are just over 10 million tracers in the spherical annulus domain. Tracers are associated with both regular mantle and primordial material and are advected following a 4th order Runge-Kutta method. The compositional field is inferred from the concentration, C, of particles of primordial material in each cell. This field takes on values between 0 for a cell filled with regular material only and 1 for a cell filled with primordial material only. Specifying the exact composition of regular mantle material and primordial material is not needed to calculate the evolution of dense material. Nevertheless, we assume that regular mantle material is pyrolytic and that the primordial material is enriched in iron oxide and bridgmanite.

In our models, the initial distribution of primordial material is contained within a uniform layer on top of the CMB with thickness, h_{DL}, which corresponds to a volume fraction, X_{prim}, given by

$$h_{DL} = \frac{[X_{prim}(1 - f^3) + f^3]^{1/3} - f}{1 - f}. \tag{D.1}$$

Using $f = 0.55$, the non-dimensional thickness of the dense layer in our model is 0.05514, which corresponds to the bottom 160 km of the lower mantle and a volume fraction of 3%.

Appendix E. Derived quantities

In this study, all observable physical parameters are averaged over a 1 Gyr window centered about $t = 4.5$ Gyr (presented in Table 2). We derive some additional physical parameters such as average height and the mean density anomalies of primordial material below.

The average height of primordial material, h_C, is considered as an indication of efficient mixing of primordial material in the mantle. This height is calculated using a volumetric integral weighted by the concentration of primordial material,

$$h_C = \int_V (r - r_{CMB}) C(r, \phi) dV \Big/ \int_V C(r, \phi) dV. \tag{E.1}$$

Average height of primordial material is bound from below by a minimum value, $h_{C,min} = h_{DL}/2$, where h_{DL} is the initial thickness of the thermochemical reservoir, and bound from above by a maximum value (when primordial material is completely mixed) given by

$$h_{C,max} = D \times \frac{\left(\frac{1 + f^3}{2} \right)^{1/3} - f}{1 - f}. \tag{E.2}$$

Here, $h_{C,min} = 80$ km and $h_{C,max} = 1830$ km. We also consider other mean heights of primordial material for $C(r, \phi)$ within specific ranges. Minor enrichment of dense material with $C(r, \phi) \leq 0.02$ is useful for monitoring the onset of slow mixing of primordial material into regular mantle material. A moderate enrichment of dense material with $C(r, \phi) \leq 0.90$ and > 0.02 is useful for monitoring the rapid entrainment of primordial material. This value range characterizes a thin veneer of primordial material with $C(r, \phi) \leq 0.90$ that surrounds the thermochemical reservoirs. The rapid uplift of this material typically precedes the onset of entrainment. Finally, dense material with $C(r, \phi) > 0.90$ characterizes the thermochemical piles. While some of this material can be rapidly entrained, the bulk concentration will be localized near the CMB. The timing of the onset of the entrainment of dense material, $t_{inst.}$, can be computed from the timing of the maximum of the second derivative of $h_{C \leq 0.9}$ and is confirmed by observing the deviation of $h_{C \leq 0.9}$ from $h_{C \geq 0.9}$ or h_C from $h_{C \geq 0.9}$.

The density anomalies of primordial material, $(d\rho/\rho)_{z,prim}$, are calculated relative to the horizontally averaged density. At each depth in the mantle, the density difference of the primordial field is calculated ($d\rho = \rho_{prim} - \bar{\rho}_z$). The average density anomaly is then calculated with respect to the density value of each point at a given depth so that

$$(d\rho/\rho)_{z,prim} = \int_{S_z} \frac{\rho_{prim} - \bar{\rho}_z}{\rho_{prim}} dS_z \Big/ \int_{S_z} dS_z \tag{E.3}$$

where dS_z is an infinitesimal spherical surface element of a spherical shell at height z above the CMB. Monitoring the density profile of primordial material clarifies its distribution throughout the mantle depth.

Appendix F. Supplementary material

Supplementary material related to this article can be found online at https://doi.org/10.1016/j.epsl.2024.118699.

References

Arevalo Jr, R., McDonough, W.F., Luong, M., 2009. The K/U ratio of the silicate Earth: Insights into mantle composition, structure and thermal evolution. Earth Planet. Sci. Lett. 278 (3–4), 361–369.

Arevalo Jr, R., McDonough, W.F., Stracke, A., Willbold, M., Ireland, T.J., Walker, R.J., 2013. Simplified mantle architecture and distribution of radiogenic power. Geochem. Geophys. Geosyst. 14 (7), 2265–2285.

Chang, Y.Y., Hsieh, W.P., Tan, E., Chen, J., 2017. Hydration-reduced lattice thermal conductivity of olivine in Earth's upper mantle. Proc. Natl. Acad. Sci. 114 (16), 4078–4081.

Citron, R.I., Lourenço, D.L., Wilson, A.J., Grima, A.G., Wipperfurth, S.A., Rudolph, M.L., et al., 2020. Effects of heat-producing elements on the stability of deep mantle thermochemical piles. Geochem. Geophys. Geosyst. 21 (4), e2019GC008895.

Cottaar, S., Lekic, V., 2016. Morphology of seismically slow lower-mantle structures. Geophys. Suppl. Mon. Not. R. Astron. Soc. 207 (2), 1122–1136.

Dalton, D.A., Hsieh, W.P., Hohensee, G.T., Cahill, D.G., Goncharov, A.F., 2013. Effect of mass disorder on the lattice thermal conductivity of MgO periclase under pressure. Sci. Rep. 3 (1), 1–5.

Davaille, A., 1999. Simultaneous generation of hotspots and superswells by convection in a heterogeneous planetary mantle. Nature 402 (6763), 756–760.

Davaille, A., Romanowicz, B., 2020. Deflating the LLSVPs: bundles of mantle thermochemical plumes rather than thick stagnant "piles". Tectonics 39 (10), e2020TC006265. https://doi.org/10.1029/2020TC006265.

Deschamps, F., Rogister, Y., Tackley, P.J., 2018. Constraints on core–mantle boundary topography from models of thermal and thermochemical convection. Geophys. J. Int. 212 (1), 164–188.

Deschamps, F., Konishi, K., Fuji, N., Cobden, L., 2019. Radial thermo-chemical structure beneath Western and Northern Pacific from seismic waveform inversion. Earth Planet. Sci. Lett. 520, 153–163.

Deschamps, F., Hsieh, W.P., 2019. Lowermost mantle thermal conductivity constrained from experimental data and tomographic models. Geophys. J. Int. 219 (Supplement), S115–S136.

Deschamps, F., Cobden, L., Tackley, P.J., 2012. The primitive nature of large low shear-wave velocity provinces. Earth Planet. Sci. Lett. 349, 198–208. https://doi.org/10.1016/j.epsl.2012.07.012.

Flament, N., Bodur, Ö.F., Williams, S.E., Merdith, A.S., 2022. Assembly of the basal mantle structure beneath Africa. Nature 603 (7903), 846–851. https://doi.org/10.1038/s41586-022-04538-y.

French, S.W., Romanowicz, B.A., 2014. Whole-mantle radially anisotropic shear velocity structure from spectral-element waveform tomography. Geophys. J. Int. 199 (3), 1303–1327.

Garnero, E.J., McNamara, A.K., Shim, S.H., 2016. Continent-sized anomalous zones with low seismic velocity at the base of Earth's mantle. Nat. Geosci. 9 (7), 481–489.

Gale, A., Dalton, C.A., Langmuir, C.H., Su, Y., Schilling, J.G., 2013. The mean composition of ocean ridge basalts. Geochem. Geophys. Geosyst. 14 (3), 489–518.

Geballe, Z.M., Sime, N., Badro, J., van Keken, P.E., Goncharov, A.F., 2020. Thermal conductivity near the bottom of the Earth's lower mantle: measurements of pyrolite up to 120 GPa and 2500 K. Earth Planet. Sci. Lett. 536, 116161.

Goncharov, A.F., Haugen, B.D., Struzhkin, V.V., Beck, P., Jacobsen, S.D., 2008. Radiative conductivity in the Earth's lower mantle. Nature 456 (7219), 231–234.

Goncharov, A.F., Lobanov, S.S., Tan, X., Hohensee, G.T., Cahill, D.G., Lin, J.F., et al., 2015. Experimental study of thermal conductivity at high pressures: implications for the deep Earth's interior. Phys. Earth Planet. Inter. 247, 11–16.

Guerrero, J.M., Deschamps, F., Li, Y., Hsieh, W.P., Tackley, P.J., 2023. Influence of heterogeneous thermal conductivity on the long-term evolution of the lower-mantle thermochemical structure: implications for primordial reservoirs. Solid Earth 14 (2), 119–135.

Hernlund, J.W., Tackley, P.J., 2008. Modeling mantle convection in the spherical annulus. Phys. Earth Planet. Inter. 171 (1–4), 48–54.

Hofmeister, A.M., 1999. Mantle values of thermal conductivity and the geotherm from phonon lifetimes. Science 283 (5408), 1699–1706.

Hsieh, W.P., Deschamps, F., Okuchi, T., Lin, J.F., 2017. Reduced lattice thermal conductivity of Fe-bearing bridgmanite in Earth's deep mantle. J. Geophys. Res., Solid Earth 122 (7), 4900–4917.

Hsieh, W.P., Deschamps, F., Okuchi, T., Lin, J.F., 2018. Effects of iron on the lattice thermal conductivity of Earth's deep mantle and implications for mantle dynamics. Proc. Natl. Acad. Sci. 115 (16), 4099–4104.

Huang, M., Li, Y., Zhao, L., 2022. Effects of thermal, compositional and rheological properties on the long-term evolution of large thermochemical piles of primordial material in the deep mantle. Sci. China Earth Sci., 1–12.

Javoy, M., Kaminski, E., Guyot, F., Andrault, D., Sanloup, C., Moreira, M., et al., 2010. The chemical composition of the Earth: enstatite chondrite models. Earth Planet. Sci. Lett. 293 (3–4), 259–268.

Jarvis, G.T., Glatzmaierand, G.A., Vangelov, V.I., 1995. Effects of curvature, aspect ratio and plan form in two- and three-dimensional spherical models of thermal convection. Geophys. Astrophys. Fluid Dyn. 79 (1–4), 147–171.

Kellogg, L.H., Hager, B.H., van der Hilst, R.D., 1999. Compositional stratification in the deep mantle. Science 283 (5409), 1881–1884.

Keppler, H., Dubrovinsky, L.S., Narygina, O., Kantor, I., 2008. Optical absorption and radiative thermal conductivity of silicate perovskite to 125 gigapascals. Science 322 (5907), 1529–1532.

Klemens, P.G., 1960. Thermal resistance due to point defects at high temperatures. Phys. Rev. 119 (2), 507.

Koelemeijer, P., Deuss, A., Ritsema, J., 2017. Density structure of Earth's lowermost mantle from Stoneley mode splitting observations. Nat. Commun. 8 (1), 15241.

Korenaga, J., 2008. Urey ratio and the structure and evolution of Earth's mantle. Rev. Geophys. 46 (2).

Lau, H.C., Mitrovica, J.X., Davis, J.L., Tromp, J., Yang, H.Y., Al-Attar, D., 2017. Tidal tomography constrains Earth's deep-mantle buoyancy. Nature 551 (7680), 321–326.

Li, M., McNamara, A.K., 2013. The difficulty for subducted oceanic crust to accumulate at the Earth's core-mantle boundary. J. Geophys. Res., Solid Earth 118 (4), 1807–1816.

Li, M., McNamara, A.K., 2022. Evolving morphology of crustal accumulations in Earth's lowermost mantle. Earth Planet. Sci. Lett. 577, 117265.

Li, Y., Deschamps, F., Tackley, P.J., 2014. The stability and structure of primordial reservoirs in the lower mantle: insights from models of thermochemical convection in three-dimensional spherical geometry. Geophys. J. Int. 199 (2), 914–930.

Li, Y., Deschamps, F., Shi, Z., Guerrero, J.M., Hsieh, W.P., Tackley, P.J., 2022. Influence of composition-dependent thermal conductivity on the long-term evolution of primordial reservoirs in Earth's lower mantle. Earth Planets Space 74, 46. https://doi.org/10.1186/s40623-022-01608-3.

Limare, A., Jaupart, C., Kaminski, E., Fourel, L., Farnetani, C.G., 2019. Convection in an internally heated stratified heterogeneous reservoir. J. Fluid Mech. 870, 67–105.

Manthilake, G.M., de Koker, N., Frost, D.J., McCammon, C.A., 2011. Lattice thermal conductivity of lower mantle minerals and heat flux from Earth's core. Proc. Natl. Acad. Sci. 108 (44), 17901–17904.

Mosca, I., Cobden, L., Deuss, A., Ritsema, J., Trampert, J., 2012. Seismic and mineralogical structures of the lower mantle from probabilistic tomography. J. Geophys. Res., Solid Earth 117 (B6).

Murakami, M., Goncharov, A.F., Miyajima, N., Yamazaki, D., Holtgrewe, N., 2022. Radiative thermal conductivity of single-crystal bridgmanite at the core-mantle boundary with implications for thermal evolution of the Earth. Earth Planet. Sci. Lett. 578, 117329.

Ohta, K., Yagi, T., Taketoshi, N., Hirose, K., Komabayashi, T., Baba, T., et al., 2012. Lattice thermal conductivity of MgSiO3 perovskite and post-perovskite at the core-mantle boundary. Earth Planet. Sci. Lett. 349, 109–115.

Resovsky, J., Trampert, J., 2003. Using probabilistic seismic tomography to test mantle velocity-density relationships. Earth Planet. Sci. Lett. 215 (1–2), 121–134.

Richter, F.M., 1985. Models for the Archean thermal regime. Earth Planet. Sci. Lett. 73 (2–4), 350–360.

Samuel, H., Farnetani, C.G., 2003. Thermochemical convection and helium concentrations in mantle plumes. Earth Planet. Sci. Lett. 207 (1–4), 39–56.

Šrámek, O., McDonough, W.F., Kite, E.S., Lekić, V., Dye, S.T., Zhong, S., 2013. Geophysical and geochemical constraints on geoneutrino fluxes from Earth's mantle. Earth Planet. Sci. Lett. 361, 356–366.

Tackley, P.J., 1998. Three-dimensional simulations of mantle convection with a thermochemical basal boundary layer: D. In: The Core-Mantle Boundary Region. In: Geodyn. Ser., vol. 28, pp. 231–253.

Tackley, P.J., King, S.D., 2003. Testing the tracer ratio method for modeling active compositional fields in mantle convection simulations. Geochem. Geophys. Geosyst. 4 (4).

Tackley, P.J., 2008. Modelling compressible mantle convection with large viscosity contrasts in a three-dimensional spherical shell using the Yin-Yang grid. Phys. Earth Planet. Inter. 171 (1), 7–18.

Tackley, P.J., 2012. Dynamics and evolution of the deep mantle resulting from thermal, chemical, phase and melting effects. Earth-Sci. Rev. 110 (1–4), 1–25. https://doi.org/10.1016/j.earscirev.2011.10.001.

Trampert, J., Deschamps, F., Resovsky, J., Yuen, D., 2004. Probabilistic tomography maps chemical heterogeneities throughout the lower mantle. Science 306 (5697), 853–856.

Turcotte, D.L., Schubert, G., 2014. Geodynamics. Cambridge University Press.

van der Hilst, R.D., Kárason, H., 1999. Compositional heterogeneity in the bottom 1000 kilometers of Earth's mantle: toward a hybrid convection model. Science 283 (5409), 1885–1888.

Xu, Y., Shankland, T.J., Linhardt, S., Rubie, D.C., Langenhorst, F., Klasinski, K., 2004. Thermal diffusivity and conductivity of olivine, wadsleyite and ringwoodite to 20 GPa and 1373 K. Phys. Earth Planet. Inter. 143, 321–336.

Zhang, Y., Yoshino, T., Yoneda, A., Osako, M., 2019. Effect of iron content on thermal conductivity of olivine with implications for cooling history of rocky planets. Earth Planet. Sci. Lett. 519, 109–119.

Zhang, Y., Yoshino, T., Osako, M., 2023. Effect of iron content on thermal conductivity of ferropericlase: implications for planetary mantle dynamics. Geophys. Res. Lett. 50 (7), e2022GL101769.